Catalysis
Science &
Technology

ROYAL SOCIETY
OF CHEMISTRY

PAPER

View Article Online
View Journal | View Issue

Check for updates

Cite this: *Catal. Sci. Technol.*, 2026, **16**, 3269

Received 5th December 2025,
Accepted 14th March 2026

DOI: 10.1039/d5cy01487e

rsc.li/catalysis

Electronic structure modulation of a Mo-doped NiO/Ni bifunctional electrocatalyst for efficient urea-assisted water splitting

Shahid Khan, Yang Lina, Yafei Feng, Mingyu Cheng,
Nazir Ahmad and Genqiang Zhang *

Urea oxidation-assisted hydrogen production provides an energy-efficient and sustainable alternative to conventional water electrolysis by significantly reducing the required cell voltage. However, developing bifunctional catalysts with high activity, long-term stability and bifunctionality remains an ongoing challenge. Here, the electronic structure of NiO/Ni is precisely modulated through molybdenum (Mo) incorporation, enabling simultaneous enhancement of the hydrogen evolution reaction (HER) and urea oxidation reaction (UOR). The resulting Mo–NiO/Ni catalyst, obtained *via* simple electrodeposition followed by an annealing approach, exhibits outstanding activity and durability, requiring cell voltages of 1.33 and 1.62 V to achieve 10 and 100 mA cm^{-2}, respectively, for overall urea electrolysis, which are 170 and 200 mV lower than those of overall water electrolysis under the same conditions. Density functional theory (DFT) calculations reveal that Mo doping optimizes the electronic configuration of NiO/Ni, lowers the activation barrier of urea dehydrogenation and approaches thermoneutral hydrogen adsorption. This work demonstrates an effective electronic structure engineering strategy for designing efficient bifunctional catalysts toward low-energy hydrogen production coupled with urea degradation.

1. Introduction

Urea-assisted water splitting is emerging as an efficient and sustainable strategy for green hydrogen production.[1] Compared with conventional steam reforming and coal gasification, electrocatalytic water splitting offers advantages of zero carbon emissions, high product purity, and low cost.[2] Replacing the sluggish, high-potential oxygen evolution reaction (OER, 1.23 V) with the UOR, (0.37 V *vs.* RHE) can markedly reduce the energy input required for hydrogen generation.[3–9] However, the complex six-electron-transfer pathway and multiple intermediates in the UOR still limit practical urea-assisted H_2 production,[6,10,11] highlighting the need for highly active bifunctional electrocatalysts to overcome kinetic barriers and enable efficient hydrogen generation.

Noble-metal catalysts such as Pt, IrO_2, and RuO_2 exhibit excellent intrinsic activity toward both the HER and UOR. However, their high cost, scarcity, and limited long-term stability severely hinder large-scale deployment in sustainable hydrogen production.[12–14] Consequently, intensive efforts have focused on developing efficient, naturally occurring, inexpensive metal-based catalysts, particularly bifunctional systems for the HER and UOR. To date, a variety of cheap transition metal catalysts composed of oxides, hydroxides, sulfides, nitrides, selenides, phosphides, *etc.* have been explored for water and urea electrolysis.[15–20] Among these, heteroatom doping has proven especially effective, as it can modulate the d-band center, increase the density of states adjacent to the Fermi level, and thereby optimize intermediate adsorption and electron transfer.[21,22] Constructing nitride–hydroxide and oxide heterostructures such as NiFe-LDH/Ni_3N and NdNiO–NiO interfaces, and C-doping into NiO have been demonstrated to enhance electrochemical performance by facilitating charge transfer, promoting active NiOOH formation and modulating local coordination environments.[23–25] For instance, Zhao *et al.* constructed a NiFe-LDH/Ni_3N heterostructure that enables rapid electron transfer and stabilizes active NiOOH species, markedly improving the HER and UOR efficiency. Their findings emphasizes the importance of nitride–hydroxide interfacial coupling in tuning electronic structure and enhancing catalytic performance.[23] Rao *et al.* designed a $NdNiO_3$–NiO heterostructure interface that promotes charge redistribution and accelerates NiOOH formation, significantly

---

Hefei National Research Center for Physical Sciences at the Microscale, CAS Key Laboratory of Materials for Energy Conversion Department of Materials Science and Engineering, University of Science and Technology of China, Hefei, Anhui 230026, P. R. China. E-mail: gqzhangmse@ustc.edu.cn

enhancing UOR activity.[24] Kou *et al.* indicated that C-doped NiO might alter the local structure of NiO and diminish the Ni coordination number, hence enhancing H* adsorption.[25] In addition, Ni, Co, and Mo-based compounds are widely investigated as HER/UOR catalysts due to their suitable electronic configurations, natural abundance, and low cost.[6,26–30] Inspired by these insights, incorporating foreign atoms into transition metal oxides offers a practical strategy to optimize their electronic structure for bifunctional electrocatalysis; nevertheless, Mo-doped NiO/Ni interfaces designed as truly bifunctional catalysts for both the HER and UOR, supported by combined experimental and DFT evidence of Mo-induced electronic modulation, remain largely underexplored.

In this work, we report a molybdenum-doped NiO/Ni (Mo–NiO/Ni) bifunctional electrocatalyst grown on nickel foam (NF) by simple electrodeposition followed by annealing. Unlike bulk Ni–Mo–O/NiMoO$_x$ catalysts (*e.g.*, NiMoO$_4$/NiMoO$_x$), our material has a Mo-doped NiO/Ni interfacial architecture, where Mo primarily acts as an electronic modulator of the NiO/Ni interface rather than forming a separate mixed-oxide phase.[31–33] By incorporating Mo to tune

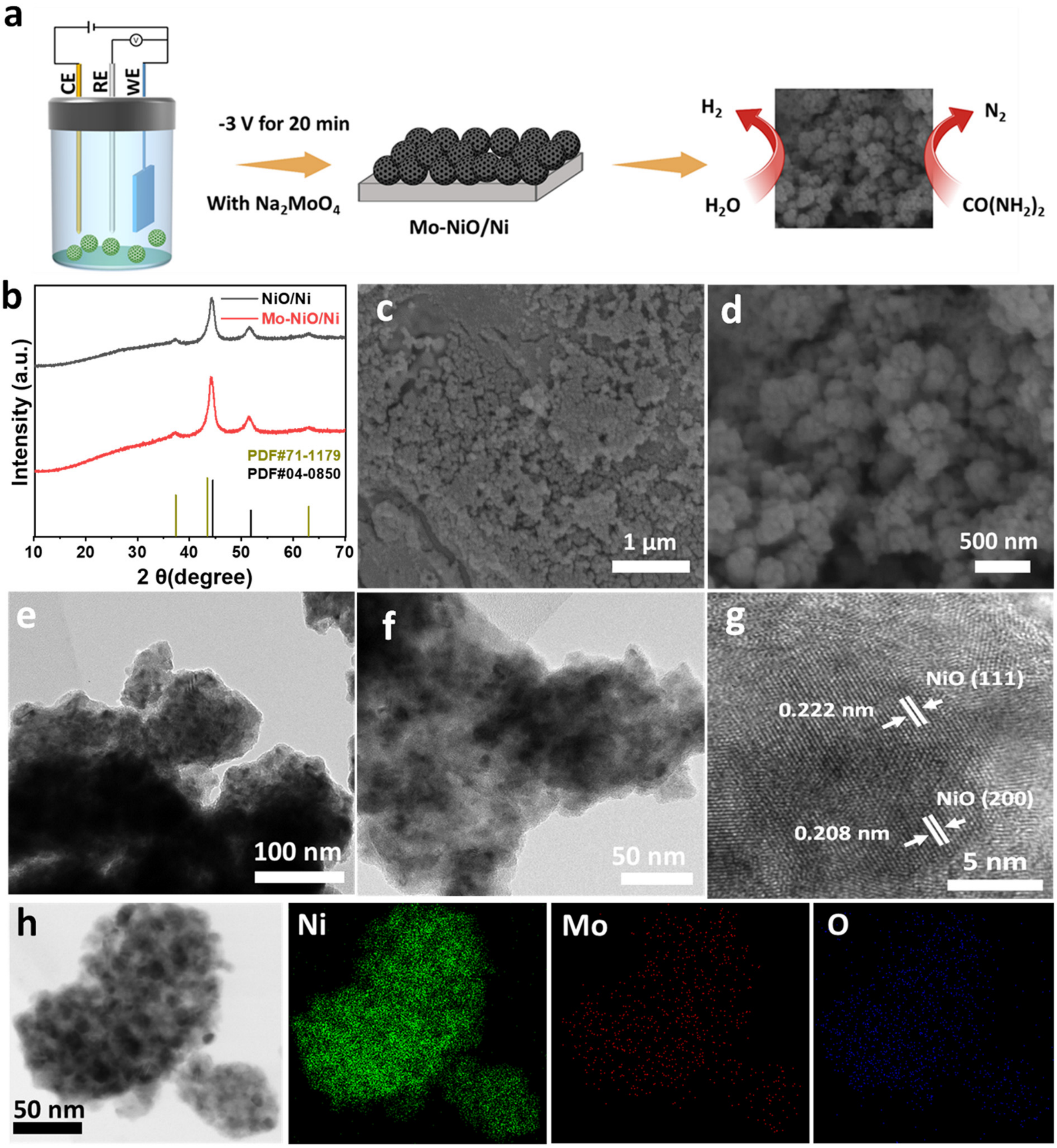

Fig. 1 (a) Schematic diagram for the synthesis of the Mo–NiO/Ni catalyst. (b) XRD analysis. (c and d) SEM. (e and f) TEM. (g) HRTEM analysis. (h) Elemental mapping.

the electronic structure at the NiO/Ni interface, the catalyst is designed to efficiently promote both the HER and the UOR in alkaline media using only earth-abundant, low-cost components. Importantly, it can deliver 10 and 100 mA cm^{-2} at 1.33 and 1.62 V using a two-electrode configuration for urea electrolysis, respectively, which are superior as compared to overall water splitting (1.5 V and 1.82 at 10 and 100 mA cm^{-2}). We propose that Mo incorporation tailors the local coordination and charge distribution, improving conductivity, increasing the density of accessible active sites, approaching thermoneutral hydrogen adsorption, and lowering the energy barrier for urea dehydrogenation, thereby enabling urea electrolysis at reduced cell voltages with sustained long-term stability.

2. Results and discussion

2.1. Synthesis and characterization

The Mo–NiO/Ni catalyst was fabricated through a one-step electrodeposition strategy as depicted in Fig. 1a, followed by annealing in an Ar/H_2 atmosphere at 450 °C for 2 hours. Unless otherwise stated, all electrodes were prepared on identical NF pieces (1 × 1 cm^2) using the same electrodeposition parameters (−3 V, 20 min) and the same exposed geometric test area (0.25 cm^2), ensuring direct comparability. NiO/Ni was synthesized using the same technique but without adding a dopant source. The crystalline structure of the prepared samples was characterized using X-ray diffraction (XRD). As shown in Fig. 1b, all the diffraction peaks of both samples are attributed to NiO (JCPDS card No. 71-1179) with no impurity phases detected (*e.g.*, crystalline $NiMoO_4$/$NiMoO_x$). The reflections from the Ni foam substrate are also present but are not labelled for clarity, and the peaks from the deposited layer are indexed to NiO. The microstructures of both samples were studied using field-emission scanning electron microscopy (FESEM), transmission electron microscopy (TEM), and high-resolution TEM (HRTEM). FESEM images of pristine NiO/Ni (Fig. S1) display a relatively smooth and compact morphology composed of loose nanoparticles, indicating limited surface roughness and lower porosity. In contrast, the Mo–NiO/Ni catalyst exhibits a markedly different surface architecture characterized by highly rough nanoparticles as shown in Fig. 1c and d. This structural evolution suggests that the introduction of Mo atoms alters the nucleation and growth behavior. The TEM images of Mo–NiO/Ni further reveal the densely packed nanoparticles as depicted in Fig. 1e and f, confirming their intimate interfacial contact. This structure revealed in TEM is expected to provide abundant exposed active sites, enhanced ion diffusion and improved electrical conductivity. The high-resolution TEM (HRTEM) image of Mo–NiO/Ni in Fig. 1g displays lattice fringes with interplanar spacings of 0.22 and 0.21 nm, consistent with the (111) and (200) planes of NiO, respectively, in good agreement with the XRD results. Moreover, the energy-dispersive spectroscopy (EDS) mapping in Fig. 1h confirms the uniform elemental dispersion of nickel (Ni), molybdenum (Mo) and oxygen (O) throughout the nanoparticles, highlighting the effect of Mo doping with NiO/Ni. The Raman spectra demonstrate clear Mo-induced modifications in the NiO lattice as depicted in Fig. S2. The Mo–NiO/Ni sample shows a strong band near 900–1000 cm^{-1} and enhanced features at 400–700 cm^{-1}, corresponding to Ni–O–Mo interactions consistent with Ni–O–Mo bonding from highly dispersed/amorphous Mo–O species, rather than a bulk $NiMoO_x$ phase. These changes indicate that Mo doping alters the local bonding, lattice symmetry and defect structure, thereby tuning the material redox and catalytic properties.[34]

X-ray photoelectron spectra (XPS) of NiO/Ni and Mo–NiO/Ni were analyzed to discover the influence of Mo-doping on the electronic configuration of NiO/Ni. The XPS survey spectrum of Mo–NiO/Ni validates the existence of Ni, O and Mo, while that of NiO/Ni confirms the presence of Ni and O as illustrated in Fig. S3. The high-resolution Ni 2p spectra show that the peaks located at 852.4 and 868.3 eV are assigned to Ni^0, while the peaks located at 855.82 and 873.46 eV with satellite peaks are ascribed to Ni^{2+} as shown in Fig. 2a.[35] Notably, the Ni 2p binding energies in Mo–NiO/Ni shift positively by 0.47 eV, which confirms that Mo doping has an effect on the electronic structure of NiO/Ni. This shift supports interfacial electronic modulation by Mo doping rather than formation of a separate bulk Ni–Mo–O ($NiMoO_x$) phase. The O 1s spectrum shows lattice oxygen (530.86 eV) and a surface-adsorbed oxygen/hydroxyl component (532.83 eV), indicating defect concentration in Mo–NiO/Ni as depicted in Fig. 2b.[36] The high-resolution Mo 3d spectrum in Fig. 2c demonstrates the simultaneous presence of Mo^{5+} and Mo^{6+} oxidation states in the Mo–NiO/Ni interface. The observed peaks at 229.9 eV and 233.1 eV correspond to Mo^{5+}, while those at 232.3 eV and 235.5 eV are assigned to Mo^{6+} components.[37] The C 1s XPS spectra show three characteristic carbon components C–C at 284.8 eV, C–O–C at 285.4 eV and C=O at 288.4 eV as illustrated in Fig. 2d. Both NiO/Ni and Mo–NiO/Ni exhibit these peaks, indicating typical surface carbon species from air exposed or synthesis residues.[38] Such mixed-valence behavior reflects electronic coupling between Mo and Ni species, which may contribute to enhanced charge transport and catalytic activity. Collectively, these XPS results validate the successful incorporation of Mo into the NiO/Ni lattice and reveal related electronic and local structural modulation features that are conducive to enhanced bifunctional HER and UOR electrocatalysis.

2.2. Electrochemical study of the HER

To evaluate the impact of Mo doping on the polarization curves of NiO/Ni, the HER activity of the as-prepared catalysts was initially assessed employing a distinctive three electrode configuration in 1 M KOH. The Hg/HgO electrode served as the reference, while the graphite rod was used as the counter

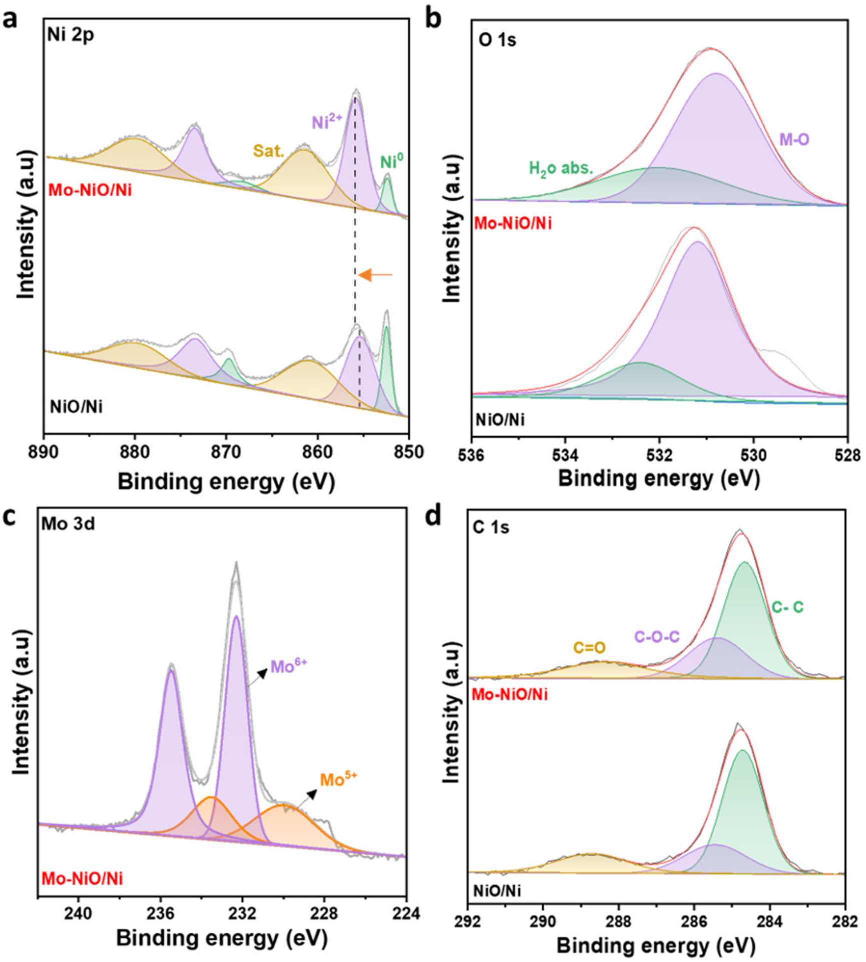

Fig. 2 High resolution XPS spectra of (a) Ni2p, (b) O 1s (c) Mo 3d and (d) C 1s.

electrode. Linear sweep voltammetry (LSV) was performed at a scan rate of 5 mV s^{-1} to examine the electrocatalytic performance. To identify the optimal catalyst, we investigated the effect of annealing temperatures on catalytic activity. Samples annealed at 400 °C, 450 °C and 500 °C were evaluated on their HER performance by electrochemical impedance spectroscopy (EIS) measurements as illustrated in Fig. S4. Among them, the catalyst annealed at 450 °C has the best HER activity. For comparison, the electrocatalytic activity of a commercial Pt–C catalyst and blank NF has been analyzed. Moreover, the LSV curves of the prepared catalyst were measured as illustrated in Fig. 3a. Notably, blank NF exhibited no electrocatalytic performance, whereas Mo–NiO/Ni shows better HER performance. As shown in Fig. S5, Mo–NiO/Ni only affords overpotentials of 51, 89, and 113 mV at current densities of 10, 50, and 100 mA cm^{-2}, respectively, which are much lower than those of NiO/Ni (97, 185 and 228 mV, respectively). Meanwhile, the η^{10} of Mo–NiO/Ni could also be compared to several recorded transition metal oxide catalysts in alkaline medium as depicted in Table S1. Specifically, as revealed in Fig. 3b, the Tafel slope of Mo–NiO/Ni is (45 mV dec^{-1}), which is much smaller than that of NiO/Ni (87 mV dec^{-1}) indicating favorable HER kinetics. Electrochemical double-layer capacitance (C_{dl}) was measured to estimate the electrochemical active surface area (ECSA) of Mo–NiO/Ni and NiO/Ni from CV measurements as depicted in Fig. S6. As shown in Fig. 3c, the calculated C_{dl} for Mo–NiO/Ni and NiO/Ni is 104 and 46 mF cm^{-2} respectively, suggesting an increased electrochemically accessible interface; however, the C_{dl} derived ECSA is only a qualitative proxy on porous/self-reconstructing NF electrodes and is therefore used here mainly for relative trend comparison. To verify the validity of the C_{dl} derived ECSA estimation, C_{dl} was measured in triplicate using independently prepared Mo–NiO/Ni electrodes under identical conditions, yielding 105, 104 and 105 mF cm^{-2} (average 104.7 mF cm^{-2}), confirming the excellent reproducibility of the C_{dl} (and hence ECSA) values (Fig. S7). The HER kinetics of Mo–NiO/Ni and NiO/Ni were evaluated by EIS. The spectra were fitted with a modified Randles circuit: $L - R_s - (R_{ct} \| CPE_{dl}) - (R_{ads} \| CPE_{ads})$.[39] Here, R_s is the solution resistance, R_{ct} is the charge-transfer resistance, CPE_{dl} represents the non-ideal double-layer capacitance, and $R_{ads} \| CPE_{ads}$ accounts for the low-frequency adsorption/desorption-related

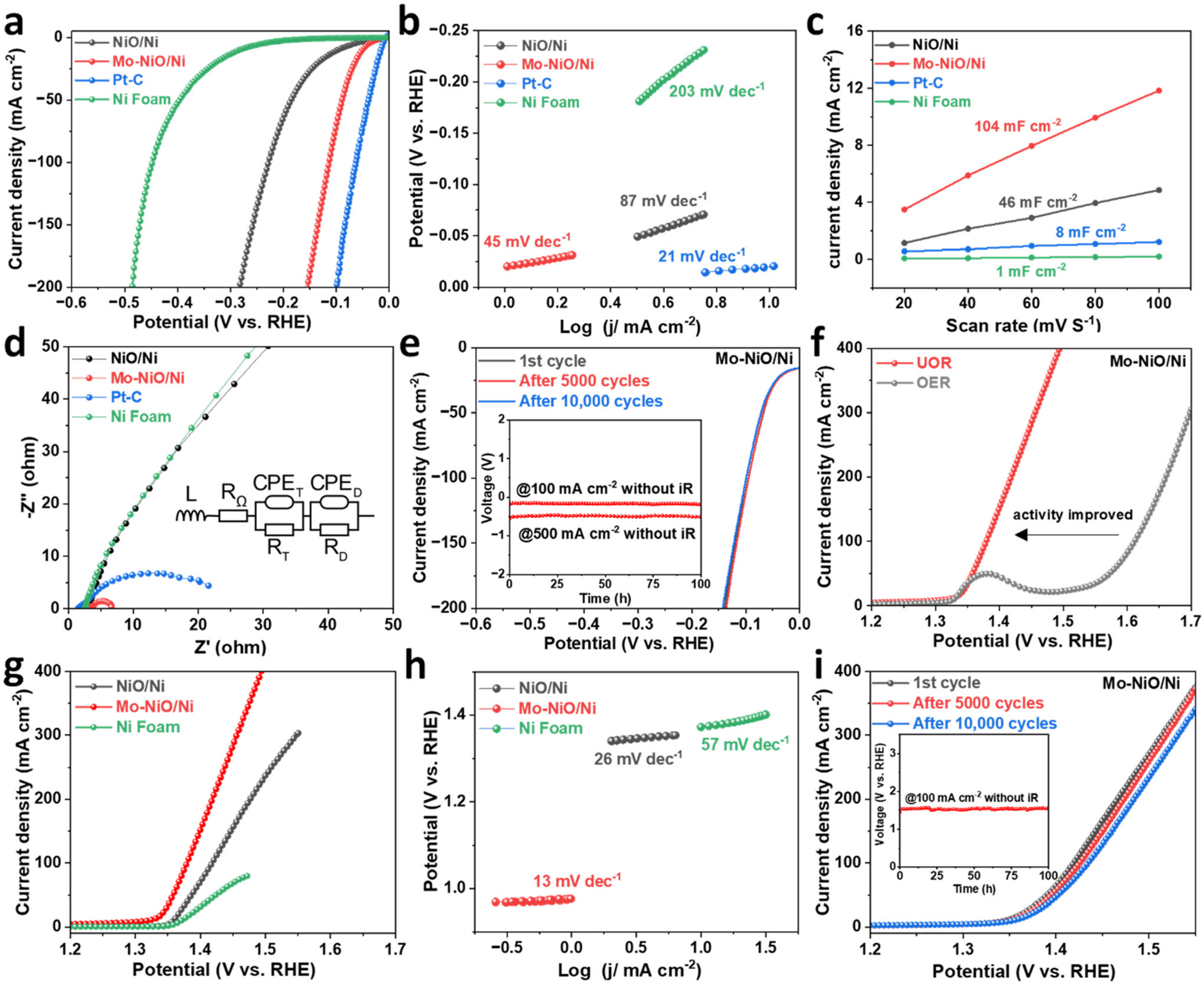

Fig. 3 Electrochemical performance evaluation of Mo–NiO/Ni. (a) Comparison of LSV curves of different catalysts for the HER. (b) Corresponding Tafel plots. (c) Double layered capacitance C_{dl} of the as-prepared catalysts. (d) Nyquist plots for the HER. (e) HER polarization curves after different CV cycles, inset is the chronopotentiometry curve at *j* of 500 and 100 mA cm^{-2}. (f) The oxidation performance comparison before and after the addition of urea. (g) LSV curves of different catalysts for the UOR. (h) Corresponding Tafel plots towards the UOR and (i) UOR polarization curves after different CV cycles, inset is the chronopotentiometry curve at current densities of 100 mA cm^{-2} without *iR* compensation.

relaxation. The series *L* term reflects high-frequency inductive effects from instrumentation. The Nyquist plots of the Mo–NiO/Ni sample exhibit a smaller R_{ct} (6.6 Ω) than the NiO/Ni sample (393 Ω), Pt–C (21.5 Ω) and Ni foam (431 Ω), indicating that Mo doping could considerably increase NiO/Ni charge transfer, as shown in Fig. 3d. We note that R_{ct} on 3D porous NF electrodes is an apparent, model-dependent parameter; therefore, we interpret the large R_{ct} decrease as a robust indicator of faster interfacial charge transfer only when consistent with the simultaneous improvements in overpotential, Tafel slope, and stability. The current density was adjusted by the ECSA to evaluate the intrinsic HER activity of the catalysts. As shown in Fig. S8, the normalized polarization curves exhibit the best HER performance of Mo–NiO/Ni. The findings propose that Mo doping boosts NiO/Ni intrinsic HER activity and catalytic active sites.

Along with catalytic activity, stability is a critical catalyst performance parameter. Thus, prolonged chronopotentiometry and CV cycles were used to determine Mo–NiO/Ni's durability in alkaline medium. Fig. 3e shows that Mo–NiO/Ni has remarkable catalytic stability, with insignificant LSV curve alterations after 5000 and 10 000 CV cycles during the HER process. Meanwhile, the stable chronopotentiometry curve recorded (inset Fig. 3e) further illustrates the robustness of Mo–NiO/Ni in the alkaline electrocatalytic system. Mo–NiO/Ni presents consistent performance over a duration of 100 h at high current densities of 500 and 100 mA cm^{-2} in separate tests. This exceptional performance highlights the promising applicability of Mo–NiO/Ni in hydrogen production.

2.3. Electrocatalytic urea oxidation reaction

The UOR activity of the as-prepared catalysts was assessed in 1 M KOH + 0.5 M urea using a standard three-electrode configuration. Remarkably, the urea amount based UOR performance of Mo–NiO/Ni was first investigated as shown in Fig. S9. It can be found that Mo–NiO/Ni attains better UOR activity at 0.5 M urea concentration. Fig. 3f shows that introducing 0.5 M urea to the electrolyte causes a substantial negative shift in the potential of Mo–NiO/Ni and a dramatic rise in current density. It should be noted that Ni-based anodes typically undergo *in situ* surface oxidation under anodic UOR polarization to form $Ni(OH)_2$/NiOOH-like species, which are widely regarded as the catalytically active surface, while the underlying NiO/Ni framework serves as a conductive scaffold.[40] In this system, the UOR needs considerably smaller potential compared to the OER, showing its inferior thermodynamic potential. Fig. 3g illustrates the electrochemical LSV curves of NF, NiO/Ni and Mo–NiO/Ni in 1 M KOH + 0.5 M urea. The Mo–NiO/Ni electrode exhibits superior electrocatalytic performance as compared to other catalysts. Specifically, the Mo–NiO/Ni electrode demonstrates anodic current densities of 10 and 100 mA cm^{-2} at 1.31 and 1.37 V *vs.* RHE, respectively. These potentials are lower than those of NiO/Ni (1.35 and 1.41 V *vs.* RHE) and NF (1.37 and 1.71 V *vs.* RHE) at the same current densities. Furthermore, this catalyst requires only 1.53 V *vs.* RHE to achieve a high current density of 500 mA cm^{-2}. Given the UOR equilibrium potential of 0.37 V *vs.* RHE, these values correspond to overpotentials of 0.94, 1.00, and 1.16 V at 10, 100, and 500 mA cm^{-2}, as depicted in Fig. S10, respectively. The Tafel plot depicted in Fig. 3h illustrates that the Tafel slope of Mo–NiO/Ni (13 mV dec^{-1}) is notably lower than that of NiO/Ni (26 mV dec^{-1}) and NF (57 mV dec^{-1}), indicating its superior electrocatalytic kinetics for the UOR. The EIS analysis provides additional evidence of the material's effective electron transfer during the UOR process (Fig. S11). In comparison to the previously published UOR catalyst, this sample exhibits a lower urea oxidation potential at a current density of 10 mA cm^{-2}, while also demonstrating more favorable kinetic performance, as illustrated in Table S2. Furthermore, we established that the optimal catalyst annealing temperature is at 450 °C for 2 hours, achieved through careful monitoring of the annealing temperature during the catalyst preparation process. For comparison, samples exposed to 400 and 500 °C were also analyzed. These samples were evaluated based on their UOR performance and electrochemical impedance characteristics during the reaction process (Fig. S12). The ECSA of the catalysts was evaluated in urea containing electrolyte, utilizing the C_{dl} derived from CV at different scan rates, as depicted in Fig. S13. The C_{dl} value for the Mo–NiO/Ni catalyst is 102 mF cm^{-2}, substantially higher than that of NiO/Ni (22 mF cm^{-2}) and Ni foam (only 1 mF cm^{-2}). Fig. 3i shows that Mo–NiO/Ni's catalytic stability during the UOR is superior, as the LSV curves show no variations after 5000 and 10 000 CV cycles. Meanwhile, the stable chronopotentiometry curve recorded (inset Fig. 3i) further illustrates the robustness of Mo–NiO/Ni in 1 M KOH + 0.5 M urea electrolyte. Mo–NiO/Ni presents a consistent performance over a duration of 100 h at a high current density of 100 mA cm^{-2}. These findings further validate the remarkable endurance of Mo–NiO/Ni in improving long-term UOR performance.

Post HER and UOR characterization was evaluated *via* XRD, SEM, and XPS. The XRD patterns (Fig. S14) retain the characteristic reflections of NiO with no new crystalline impurity phases detected, suggesting that the bulk NiO structure remains largely preserved. The morphology results obtained after the HER and UOR stability test (Fig. S15) show well-preserved confined nanoparticles, indicating the excellent mechanical stability of Mo–NiO/Ni. The XPS spectra as depicted in Fig. S16 further show that Mo–NiO/Ni exhibits favorable stability. Post-HER and UOR XPS analyses show the disappearance of the Ni^0 feature in the Ni 2p spectra and the emergence of NiO peaks in XRD patterns, indicating electrochemical surface reconstruction. Under anodic UOR conditions, the surface converts to $Ni(OH)_2$/NiOOH-like species, while the NiO/Ni structure mainly serves as a conductive support. The coexistence of Ni^{2+} species and stable Mo signals confirms that Mo remains associated with the reconstructed surface and/or subsurface, supporting its role in electronic modulation/stabilization under operation.[41] Together, these results demonstrate excellent structural and chemical stability and help rationalize the outstanding urea-assisted overall splitting activity of Mo–NiO/Ni relative to current catalysts.

2.4. Overall water and urea splitting activity

As shown in Fig. 4a, two identical Mo–NiO/Ni electrodes were used as the cathode and anode to test the practicality of water and urea splitting systems due to their strong bifunctional catalytic activity for the HER and UOR. Remarkably, this hybrid electrolyzer exhibits exceptional performance in overall urea electrolysis under alkaline conditions, as illustrated in Fig. 4b. It achieves cell voltages of 1.33 and 1.62 V to attain current densities of 10 and 100 mA cm^{-2} for urea-assisted electrolysis, compared with 1.50 and 1.82 V for overall water electrolysis under the same conditions. Thus, urea-assisted electrolysis reduces the required cell voltage by 170 mV at 10 mA cm^{-2} and 200 mV at 100 mA cm^{-2} relative to overall water splitting. Furthermore, this performance is competitive with other published electrocatalysts targeting urea-assisted water splitting, as detailed in Table S3. Moreover, elevated current densities of 50, 100, and 150 mA cm^{-2} are easily achieved at lower voltages of 1.51, 1.62 and 1.72 V, suppressing the overall water splitting system (1.7, 1.82 and 1.92 V) as depicted in Fig. 4c. This difference highlights the potential of the system for cost-effective hydrogen production and

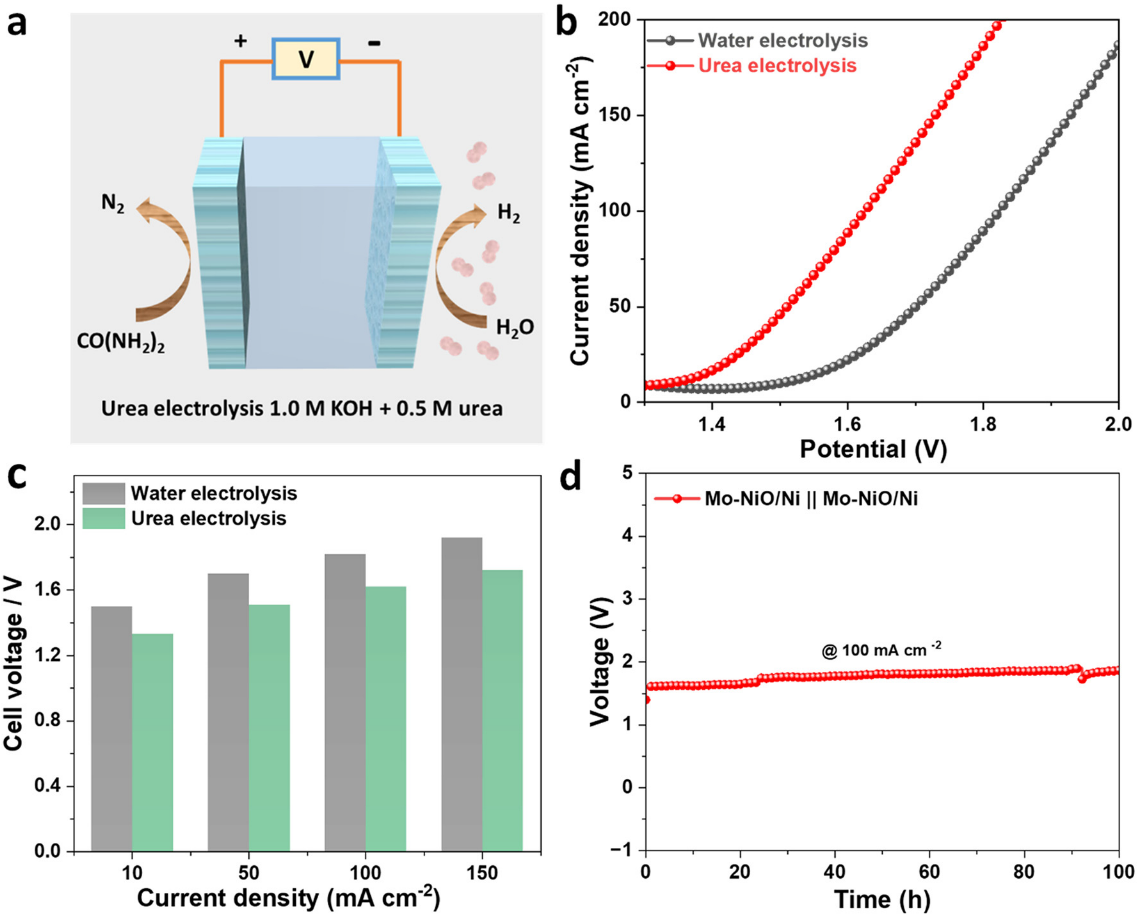

Fig. 4 (a) Schematic illustration of the two-electrode system with the Mo–NiO/Ni cathode and anode. (b) LSV curves of Mo–NiO/Ni‖Mo–NiO/Ni in 1 M KOH and 1 M KOH having 0.5 M urea. (c) Comparison of cell voltages at 10, 50, 100 and 150 mA cm^{-2} for water and urea electrolysis and (d) *i*–*t* curve at a current density of 100 mA cm^{-2}.

efficient treatment of urea-rich wastewater. Further, long-term stability is also a vital factor for the practicality of any electrocatalyst. Significantly, the Mo–NiO/Ni electrode demonstrates remarkable stability, successfully catalyzing urea electrolysis for 100 hours without a noticeable decline in current density, as shown in Fig. 4d. This observation highlights the catalyst excellent stability. Together, these results illustrate that bifunctional Mo–NiO/Ni indeed exhibits highly efficient catalytic performance in the simultaneous processes of water and urea electrolysis, making it a promising candidate for hydrogen evolution applications.

2.5. Study of the catalytic mechanism

We note that the DFT models employed here represent idealized/static NiO/Ni and Mo–NiO/Ni interfaces. They do not explicitly include *operando* reconstruction (*e.g.*, $Ni(OH)_2$/NiOOH formation), electrolyte/solvent, or applied potential; therefore, the calculations are used to provide qualitative trends in electronic redistribution and relative adsorption changes that are consistent with the experimental observations. DFT calculations were carried out to unravel the structural and electronic modulation of the NiO/Ni interface upon Mo incorporation. As illustrated in Fig. 5a and b Mo atoms are incorporated into the NiO lattice, inducing local lattice distortion and forming strong Mo–O–Ni bonds that alter the interfacial coordination environment. The corresponding charge density difference plot reveals significant electron redistribution, with pronounced electron accumulation near Mo sites and depletion around neighboring Ni atoms, indicating evident interfacial charge transfer as depicted in Fig. 5c. The PDOS of NiO/Ni (Fig. S17) exhibits dominant Ni 3d states near the Fermi level and strong Ni–O hybridization, consistent with partial metallicity at the interface. In contrast, Mo doping introduces additional Mo 4d electronic states near the Fermi level, effectively enhancing electronic conductivity and improving Mo–Ni–O hybridization, as illustrated in Fig. 5d. This structural and electronic regulation optimizes the surface adsorption characteristics, promoting more efficient charge transfer and intermediate stabilization during catalytic reactions. Generally, the Gibbs free energy toward hydrogen adsorption (ΔG_{H^*}) plays an important role in evaluating the HER due to simultaneous optimized hydrogen adsorption/desorption reaction.[42,43] The calculated Gibbs free energy deeper

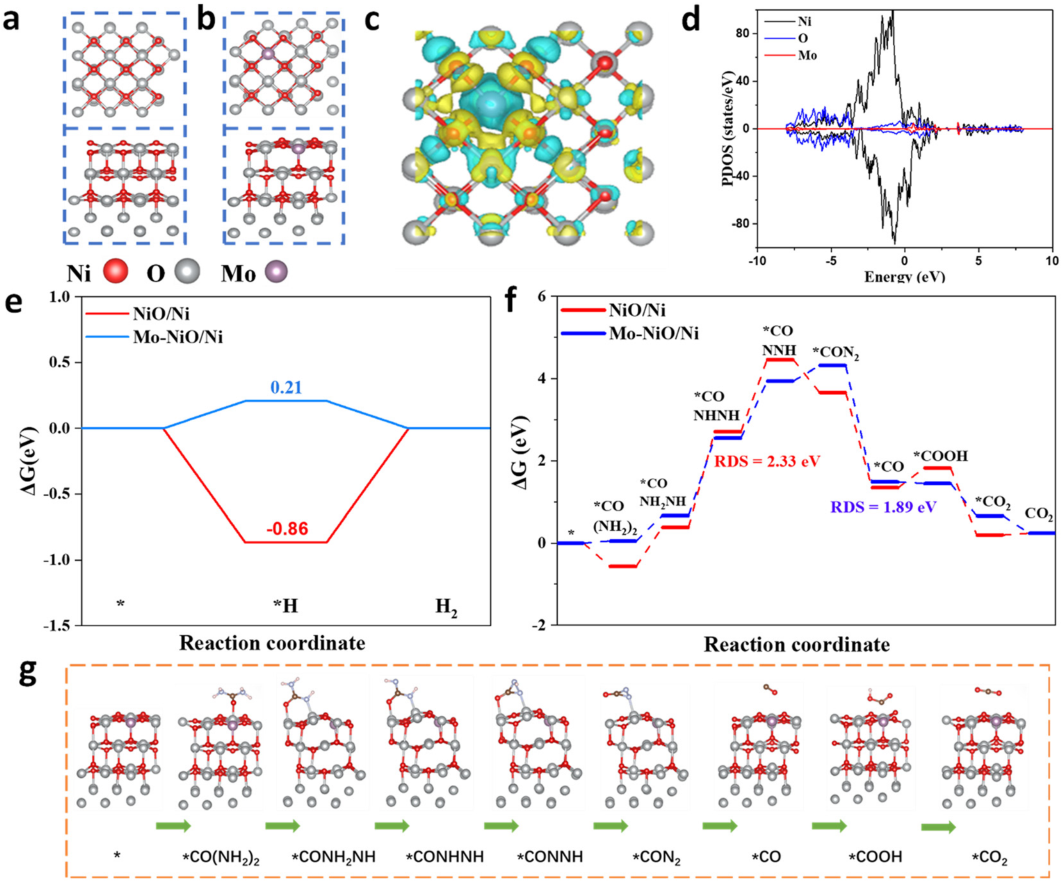

Fig. 5 DFT calculations. Top and side views of the structural models of (a) NiO/Ni and (b) Mo–NiO/Ni. (c) Differential charge density of Mo–NiO/Ni. The yellow area signifies electron accumulation, whereas the cyan area indicates electron depletion. (d) Calculated PDOS of Mo–NiO/Ni. (e) The Gibbs free energy diagram of the HER for NiO/Ni and Mo–NiO/Ni. (f) Gibbs free-energy profile for the UOR. (g) Diagrammatic representation of the urea oxidation mechanism and its associated arrangements.

insights the catalytic role of Mo. As depicted in Fig. 5e, the hydrogen adsorption free energy (ΔG_{H*}) of pristine NiO/Ni is −0.86 eV, indicating overly strong H binding, whereas Mo–NiO/Ni exhibits a near-thermoneutral ΔG_{H*} of 0.21 eV, suggesting more favorable HER kinetics. The HER structural models for NiO/Ni and Mo–NiO/Ni are illustrated in Fig. S18. This near-thermoneutral hydrogen adsorption is consistent with the low HER overpotentials (51 and 113 mV at 10 and 100 mA cm^{-2}) and the reduced Tafel slope observed experimentally. Because the UOR proceeds through multiple intermediates and parallel pathways, we use the dehydrogenation of adsorbed urea ($CO(NH_2)_2 \rightarrow CON_2$) as a representative potential-determining/rate-limiting step for comparative catalyst screening, rather than attempting to model the full *operando* network. Furthermore, the calculated UOR free energy reaction pathway as illustrated in Fig. 5f indicates that Mo doping substantially decreases the energy barrier for this representative dehydrogenation step from 2.33 eV to 1.89 eV, facilitating the conversion of $*CO(NH_2)_2$ to $*CON_2$ intermediates. This lowered barrier is qualitatively consistent with the experimentally observed trend of a lower UOR onset potential and a smaller Tafel slope for Mo–NiO/Ni relative to NiO/Ni. DFT indicates that Mo–NiO/Ni (Fig. 5g) and NiO/Ni (Fig. S19) follow the same UOR route, where adsorbed urea is stepwise dehydrogenated and oxidized ($*CO(NH_2)_2 \rightarrow *CONH_2NH \rightarrow *CONHNH \rightarrow *CONNH \rightarrow *CON_2 \rightarrow *CO \rightarrow *COOH \rightarrow *CO_2$). Compared with NiO/Ni, Mo incorporation in Mo–NiO/Ni optimizes intermediate adsorption/stabilization, thereby promoting the overall UOR process. Collectively, these theoretical insights support that Mo modification optimizes the interfacial electronic structure and energetics of NiO/Ni, thereby promoting both hydrogen evolution and urea oxidation reactivity. These results indicate that the key role of Mo is to tune the electronic structure at the NiO/Ni interface, which is fundamentally different from bulk Ni–Mo–O/NiMoO$_x$ catalysts.

Conclusion

In conclusion, we have established a simple approach for the fabrication of an effective bifunctional Mo–NiO/Ni electrocatalyst by a one-step electrodeposition process followed by annealing. Remarkably, the prepared Mo–NiO/Ni catalyst achieves superior performance and prolonged stability for the HER and UOR. The catalyst achieves HER η of 51 and 113 mV at 10 and 100 mA cm^{-2}, respectively, and a UOR potential of 1.37 V *vs.* RHE to reach 100 mA cm^{-2}. A symmetric two-electrode electrolyzer demonstrates exceptional overall water and urea splitting performance, requiring 1.62 V at 100 mA cm^{-2} in urea containing electrolyte, outperforming water electrolysis under identical conditions (1.82 V). DFT studies demonstrate that the Mo–NiO/Ni catalyst's strong bifunctional catalytic performance is mainly due to the electronic structure's modification, which improves conductivity and intermediate adsorption/desorption. Meanwhile, Mo–NiO/Ni uniformly grows on the NF and creates nanoparticles with more active sites for catalysis. This study presents a novel strategy for constructing high-performance Mo–NiO/Ni bifunctional catalysts, exhibiting significant potential for industrial water splitting and urea oxidation.

Author contributions

Shahid Khan: conceptualization, methodology, sample preparation, electrochemical testing, data analysis and manuscript preparation. Yang Lina: conducted DFT calculations. Yafei Feng: formal analysis, validation, and visualization. Mingyu Cheng: formal analysis, validation, and visualization. Nazir Ahmad: formal analysis, validation, and visualization. Genqiang Zhang: supervised the project and contributed to the experimental planning, data analysis and manuscript preparation.

Conflicts of interest

The authors declare no conflict of interest.

Data availability

The data that support the findings of this study are available from the corresponding author upon reasonable request.

Supplementary information (SI) is available. See DOI: https://doi.org/10.1039/d5cy01487e.

Acknowledgements

This work was financially supported by the National Key R&D Program of China (2022YFA1504001), the National Natural Science Foundation of China (T2325021, 22321001), and the CAS Project for Young Scientists in Basic Research (YSBR-070). The numerical calculations in this paper have been performed in the Supercomputing Center of University of Science and Technology of China.

References

1 J. Jian, Y. Qiao, F. Chen, C. Liu, W. Liu and Z. Li, *et al.* Local Charge Density Regulation of NiP2 Nanosheets via Ru Doping for Electrocatalytic Urea Oxidation, *Appl. Catal., B*, 2025, 125390.

2 H. Yu, S. Zhu, Y. Hao, Y. M. Chang, L. Li and J. Ma, *et al.* Modulating local interfacial bonding environment of heterostructures for energy-saving hydrogen production at high current densities, *Adv. Funct. Mater.*, 2023, **33**(12), 2212811.

3 W. Xiang, N. Yang, X. Li, J. Linnemann, U. Hagemann and O. Ruediger, *et al.* 3D atomic-scale imaging of mixed Co-Fe spinel oxide nanoparticles during oxygen evolution reaction, *Nat. Commun.*, 2022, **13**(1), 179.

4 X. Wang, S. Xi, P. Huang, Y. Du, H. Zhong and Q. Wang, *et al.* Pivotal role of reversible NiO6 geometric conversion in oxygen evolution, *Nature*, 2022, **611**(7937), 702–708.

5 B. Zhu, Z. Liang and R. Zou, Designing advanced catalysts for energy conversion based on urea oxidation reaction, *Small*, 2020, **16**(7), 1906133.

6 L. Wang, Y. Zhu, Y. Wen, S. Li, C. Cui and F. Ni, *et al.* Regulating the local charge distribution of Ni active sites for the urea oxidation reaction, *Angew. Chem., Int. Ed.*, 2021, **60**(19), 10577–10582.

7 X. Hu, J. Zhu, J. Li and Q. Wu, Urea electrooxidation: current development and understanding of Ni-based catalysts, *ChemElectroChem*, 2020, **7**(15), 3211–3228.

8 B. K. Boggs, R. L. King and G. G. Botte, Urea electrolysis: direct hydrogen production from urine, *Chem. Commun.*, 2009, 4859–4861.

9 S.-K. Geng, Y. Zheng, S.-Q. Li, H. Su, X. Zhao and J. Hu, *et al.* Nickel ferrocyanide as a high-performance urea oxidation electrocatalyst, *Nat. Energy*, 2021, **6**(9), 904–912.

10 H. Jiang, M. Sun, S. Wu, B. Huang, C. S. Lee and W. Zhang, Oxygen-incorporated NiMoP nanotube arrays as efficient bifunctional electrocatalysts for urea-assisted energy-saving hydrogen production in alkaline electrolyte, *Adv. Funct. Mater.*, 2021, **31**(43), 2104951.

11 A. Kumar, X. Liu, J. Lee, B. Debnath, A. R. Jadhav and X. Shao, *et al.* Discovering ultrahigh loading of single-metal-atoms via surface tensile-strain for unprecedented urea electrolysis, *Energy Environ. Sci.*, 2021, **14**(12), 6494–6505.

12 I. Roger, M. A. Shipman and M. D. Symes, Earth-abundant catalysts for electrochemical and photoelectrochemical water splitting, *Nat. Rev. Chem.*, 2017, **1**(1), 0003.

13 M. Gong and H. Dai, A mini review of NiFe-based materials as highly active oxygen evolution reaction electrocatalysts, *Nano Res.*, 2015, **8**(1), 23–39.

14 C. C. McCrory, S. Jung, J. C. Peters and T. F. Jaramillo, Benchmarking heterogeneous electrocatalysts for the oxygen evolution reaction, *J. Am. Chem. Soc.*, 2013, **135**(45), 16977–16987.

15 P. Babar, A. Lokhande, V. Karade, B. Pawar, M. G. Gang and S. Pawar, *et al.* Bifunctional 2D electrocatalysts of transition metal hydroxide nanosheet arrays for water splitting and urea electrolysis, *ACS Sustainable Chem. Eng.*, 2019, **7**(11), 10035–10043.

16 C. Xu, X. Yang, S. Li, K. Li, B. Xi and Q.-W. Han, *et al.* Modulating the electronic configuration of Co species in MOF/MXene nanosheet derived Co-based mixed spinel

oxides for an efficient oxygen evolution reaction, *Inorg. Chem. Front.*, 2023, **10**(1), 85–92.

17 W. Zhu, Z. Yue, W. Zhang, N. Hu, Z. Luo and M. Ren, *et al.* Wet-chemistry topotactic synthesis of bimetallic iron–nickel sulfide nanoarrays: an advanced and versatile catalyst for energy efficient overall water and urea electrolysis, *J. Mater. Chem. A*, 2018, **6**(10), 4346–4353.

18 N. Han, P. Liu, J. Jiang, L. Ai, Z. Shao and S. Liu, Recent advances in nanostructured metal nitrides for water splitting, *J. Mater. Chem. A*, 2018, **6**(41), 19912–19933.

19 W. Cao, Q. Shen, D. Men, B. Ouyang, Y. Sun and K. Xu, Phase engineering of iron group transition metal selenides for water splitting, *Mater. Chem. Front.*, 2023, **7**(20), 4865–4879.

20 Z. Wang, J. Yang, W. Wang, F. Zhou, H. Zhou and Z. Xue, *et al.* Hollow cobalt-nickel phosphide nanocages for efficient electrochemical overall water splitting, *Sci. China Mater.*, 2021, **64**(4), 861–869.

21 Z. Chen, Y. Song, J. Cai, X. Zheng, D. Han and Y. Wu, *et al.* Tailoring the d-band centers enables Co4N nanosheets to be highly active for hydrogen evolution catalysis, *Angew. Chem., Int. Ed.*, 2018, **57**(18), 5076–5080.

22 N. Yao, P. Li, Z. Zhou, Y. Zhao, G. Cheng and S. Chen, *et al.* Synergistically tuning water and hydrogen binding abilities over Co4N by Cr doping for exceptional alkaline hydrogen evolution electrocatalysis, *Adv. Energy Mater.*, 2019, **9**(41), 1902449.

23 J. Zhao, Y. Zhang, H. Guo, J. Ren, H. Zhang and Y. Wu, *et al.* Defect-rich Ni(OH)2/NiO regulated by WO3 as core–shell nanoarrays achieving energy-saving water-to-hydrogen conversion via urea electrolysis, *Chem. Eng. J.*, 2022, **433**, 134497.

24 N. N. Rao, C. Alex, S. Tomar, M. S. N. Kovilakath, S.-C. Lee and S. Bhattacharjee, *et al.* Interface-driven electrocatalysis: Highlighting the role of NdNiO3-NiO heterointerface in urea electro-oxidation, *Appl. Catal., B*, 2025, **371**, 125177.

25 T. Kou, M. Chen, F. Wu, T. J. Smart, S. Wang and Y. Wu, *et al.* Carbon doping switching on the hydrogen adsorption activity of NiO for hydrogen evolution reaction, *Nat. Commun.*, 2020, **11**(1), 590.

26 F. Cai, L. Liao, Y. Zhao, D. Li, J. Zeng and F. Yu, *et al.* Large-current-stable bifunctional nanoporous Fe-rich nitride electrocatalysts for highly efficient overall water and urea splitting, *J. Mater. Chem. A*, 2021, **9**(16), 10199–10207.

27 Z.-Y. Yu, C.-C. Lang, M.-R. Gao, Y. Chen, Q.-Q. Fu and Y. Duan, *et al.* Ni–Mo–O nanorod-derived composite catalysts for efficient alkaline water-to-hydrogen conversion via urea electrolysis, *Energy Environ. Sci.*, 2018, **11**(7), 1890–1897.

28 C. Wang, H. Lu, Z. Mao, C. Yan, G. Shen and X. Wang, Bimetal Schottky heterojunction boosting energy-saving hydrogen production from alkaline water via urea electrocatalysis, *Adv. Funct. Mater.*, 2020, **30**(21), 2000556.

29 X. Zhu, X. Dou, J. Dai, X. An, Y. Guo and L. Zhang, *et al.* Metallic nickel hydroxide nanosheets give superior electrocatalytic oxidation of urea for fuel cells, *Angew. Chem., Int. Ed.*, 2016, **55**(40), 12465–12469.

30 Q. He, Y. Wan, H. Jiang, Z. Pan, C. Wu and M. Wang, *et al.* Nickel vacancies boost reconstruction in nickel hydroxide electrocatalyst, *ACS Energy Lett.*, 2018, **3**(6), 1373–1380.

31 V. Maheskumar, A. Min, C. J. Moon, R. A. Senthil and M. Y. Choi, Modulating the electronic structure of Ni/NiO nanocomposite with high-valence Mo doping for energy-saving hydrogen production via boosting urea oxidation kinetics, *Small Struct.*, 2023, **4**(12), 2300212.

32 T. Wang, H. Wu, C. Feng, Y. Ding and H. Mei, Ni, N-codoped NiMoO$_4$ grown on 3D nickel foam as bifunctional electrocatalysts for hydrogen production in urea-water electrolysis, *Electrochim. Acta*, 2021, **391**, 138931.

33 T. Ali, X. Wang, K. Tang, Q. Li, S. Sajjad and S. Khan, *et al.* SnS2 quantum dots growth on MoS2: Atomic-level heterostructure for electrocatalytic hydrogen evolution, *Electrochim. Acta*, 2019, **300**, 45–52.

34 C. Yang, N. Gao, X. Wang, J. Lu, L. Cao and Y. Li, *et al.* Stable and efficient seawater splitting on a porous phosphate-intercalated NiFe (oxy) hydroxide@NiMoO4 core-shell micropillar electrode, *Energy Mater.*, 2021, **1**, 100015.

35 Y. Zhu, J. Zhang, Q. Qian, Y. Li, Z. Li and Y. Liu, *et al.* Dual nanoislands on Ni/C hybrid nanosheet activate superior hydrazine oxidation-assisted high-efficiency H2 production, *Angew. Chem., Int. Ed.*, 2022, **61**(2), e202113082.

36 K. Kotsis and V. Staemmler, Ab initio calculations of the O1s XPS spectra of ZnO and Zn oxo compounds, *Phys. Chem. Chem. Phys.*, 2006, **8**(13), 1490–1498.

37 M. Tanhaei, M. Yang, J. J. Cheng, Y. Ren, A. Nemati and J. Pan, *et al.* Enhanced CO2 sorption in a hybrid PEI-Mo oxide film via pulsed electrodeposition, *Mater. Adv.*, 2022, **3**(13), 5510–5520.

38 H. Sun, Y. Lian, C. Yang, L. Xiong, P. Qi and Q. Mu, *et al.* A hierarchical nickel-carbon structure templated by metal-organic frameworks for efficient overall water splitting, *Energy Environ. Sci.*, 2018, **11**(9), 2363–2371.

39 T. Ali, W. Qiao, D. Zhang, W. Liu, S. Sajjad and C. Yan, *et al.* Surface sulfur vacancy engineering of metal sulfides promoted desorption of hydrogen atoms for enhanced electrocatalytic hydrogen evolution, *J. Phys. Chem. C*, 2021, **125**(23), 12707–12712.

40 X. Guo, L. Qiu, M. Li, F. Tian, X. Ren and S. Jie, *et al.* Accelerating the generation of NiOOH by in-situ surface phosphating nickel sulfide for promoting the proton-coupled electron transfer kinetics of urea electrolysis, *Chem. Eng. J.*, 2024, **483**, 149264.

41 J. Luo, Y. Zhang, L. Tang, D. Lu, T. Zhang and H. Zhao, *et al.* Electrochemical self-reconstruction helps self-supported Ni3S2@ NiFeOOH-MOF/NFF electrodes to enhance electrocatalytic oxygen evolution, *Int. J. Hydrogen Energy*, 2025, **114**, 394–402.

42 Y. Li, J. Zhang, Y. Liu, Q. Qian, Z. Li and Y. Zhu, *et al.* Partially exposed RuP2 surface in hybrid structure endows its bifunctionality for hydrazine oxidation and hydrogen evolution catalysis, *Sci. Adv.*, 2020, **6**(44), eabb4197.

43 Q. Qian, Y. Li, Y. Liu and G. Zhang, General anion-exchange reaction derived amorphous mixed-metal oxides hollow nanoprisms for highly efficient water oxidation electrocatalysis, *Appl. Catal., B*, 2020, **266**, 118642.